Acta Materialia 304 (2026) 121797

Contents lists available at ScienceDirect

Acta Materialia

journal homepage: www.elsevier.com/locate/actamat

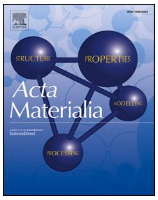

Measurement of cleavage toughness of brittle materials by local elastic field analysis

Xiao Su [a,*], Zikang Zhang [a], Marcus Williamson [a], Marin Vuksic [a], Abdalrhaman Koko [a,b], T. James Marrow [a]

[a] Department of Materials, University of Oxford, Parks Road, Oxford, OX1 3PH, UK
[b] National Physical Laboratory, Hampton Road, Teddington, TW11 0LW, UK

ARTICLE INFO

Keywords:
Fracture toughness
Full-field strain measurement
Microscale testing
HR-EBSD
Stress intensity factor
Nano-indentation

ABSTRACT

Measurement of the fracture toughness of materials at the microscale is critical for ensuring structural integrity and understanding of fracture behaviour. Existing approaches rely on simplified assumptions or complex sample preparation that challenge interpretation and reproduction. This work presents a novel method to obtain cleavage fracture toughness through measurements by high (angular) resolution electron backscatter diffraction of the critical elastic field at an arrested crack tip, achieved by double-nanoindentation. A case study in single-crystal silicon, a representative brittle material, demonstrates the reproducibility and reliability of the measurements. The potential application to investigate intergranular cleavage in brittle polycrystalline materials is discussed.

1. Introduction

Mechanical integrity at small length scales is essential in the design of materials that operate in extreme environments, such as aerospace [1–3], microelectronics [4,5] and energy storage [6,7]. Ceramics and advanced composites, which offer high performance due to their combination of low density, high hardness and thermal stability, are typically brittle with low fracture toughness at the microscale. However, controlled use of low toughness interfaces and grain boundaries [8,9] in microstructure design can remarkably improve the damage tolerance of engineering ceramics at the macroscale through crack deflection [10] and distributed microcracking [11].

Micro-mechanical testing aims to directly evaluate mechanical properties at the scale of individual microstructural features. In addition to providing critical inputs for microstructure-informed design of bulk ceramics and composites, micro-mechanical testing is essential when fracture behaviour is size-dependent or interface-dominated. Examples include coatings [12,13], solid-state battery materials [6,7,14], microelectromechanical systems (MEMS) [15], and layered electronics [4,5]. Fracture toughness measurement at these scales poses significant challenges, including the preparation of defect-free specimens with controlled geometry, the need to decouple substrate and residual stress contributions, and the difficulty of probing localised properties in complex microstructures.

The classical method to characterise fracture toughness at small length scales in brittle materials is built upon indentation techniques where the strain to accommodate a sharp nano-scale or micro-scale indenter induces controlled cracking. This offers significant advantages of experimental simplicity and minimal material requirements. The Lawn-Evans-Marshall (LEM) model [16–19] serves as a foundational analysis approach and relates the indentation load and surface crack length to the mode I fracture toughness through a semi-empirical formulation involving hardness, elastic modulus, and crack geometry. This has been effective for bulk polycrystalline ceramics, but it has intrinsic limitations at the microscale. The complex elastic strain field beneath the indenter [20], plasticity [21,22], and the indenter-dependent nature of the developed cracks [23] all introduce significant uncertainty. This is because the idealised conditions assumed, such as the formation of radial cracks under well-defined loading, can be challenging to achieve in practice. Residual stresses and substrate effects [24] also compromise the validity of this method.

To address these limitations, a new generation of microscale fracture toughness testing methods combines micro/nano-fabrication techniques (primarily focused ion beam or FIB milling) with nanoindentation loading under scanning electron microscope (SEM) observation. Representative geometries include bending of single cantilevers [25],

---

* Corresponding author.
E-mail address: xiao.su@materials.ox.ac.uk (X. Su).

https://doi.org/10.1016/j.actamat.2025.121797
Received 8 October 2025; Received in revised form 29 November 2025; Accepted 1 December 2025

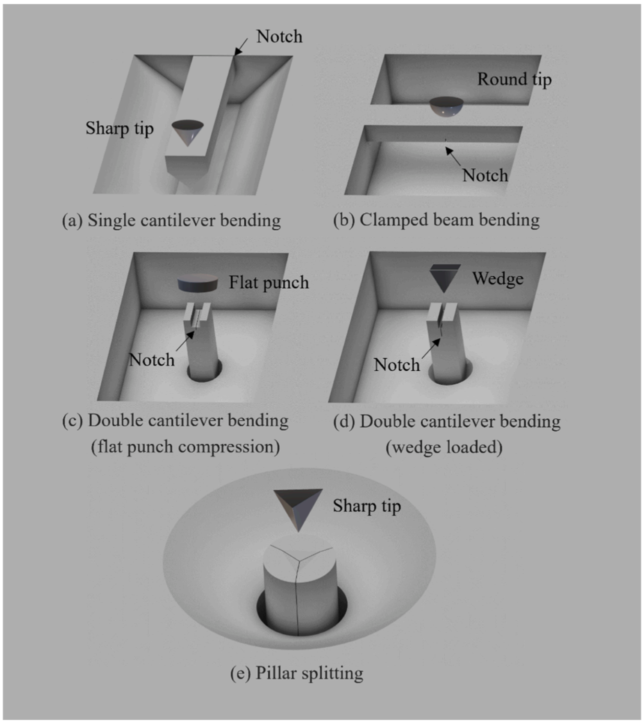

(a) Single cantilever bending

(b) Clamped beam bending

(c) Double cantilever bending (flat punch compression)

(d) Double cantilever bending (wedge loaded)

(e) Pillar splitting

Fig. 1. Schematic illustrations of microscale fracture toughness test geometries.

clamped beams [26] and double cantilevers [27,28], and pillar splitting [29] (Fig. 1). These enable localised testing of the fracture properties of micro-specimens with unprecedented spatial resolution. Critically, they allow targeting of specific microstructural features such as grain boundaries [25,30,31], interfaces [32–34], or individual phases [35,36]. However, there is a lack of established standards at this length scale and deviations from the assumed conditions of the test design can compromise the reliability of the results [37].

Microcantilever bending has been applied widely due to its versatility. It has proved effective, for example, in studies of intergranular fracture [35], radiation damage [38], and dislocation-mediated toughening [39]. For rectangular beams with a straight notch, the mode I fracture toughness can be obtained by analytical solutions, whereas more complex geometries require finite element models [23]. Despite its advantages, the method presents notable challenges since achieving pure mode I loading demands a straight crack path and symmetric bending without shear [40], and the accuracy depends on precise loading, geometry and metrology. Furthermore, ion beam-induced damage and residual stresses can modify the strain fields and fracture behaviour [12,41].

Clamped beam bending, in which both ends of a micro-beam are constrained, facilitates stable crack propagation in brittle materials. Achieving pure mode I loading requires a precisely loaded notch at the beam centre, which limits the ability to position the crack at specific microstructural features. Analytical solutions are not available for this configuration, and a finite element analysis [42] is required for each specimen. Moreover, the constrained ends can introduce artefacts such as residual stresses and secondary cracking [42].

Double cantilever bending by flat punch compression [27] can also achieve stable crack propagation. Variants, for example wedge-loaded double cantilever bending [28], have improved the stability of this geometry. However, the applied load must be symmetric and precisely aligned to achieve pure mode I conditions. Contact stresses and friction [43] can compromise the accuracy of the test and the compliance of the loading system can affect the crack stability.

The micro-pillar splitting technique applies nano-indentation on cylindrical pillars to initiate cracks that split the pillar by propagating towards its sidewalls. The critical splitting load gives the fracture toughness through a calibrated relationship that depends on the pillar geometry and material properties. Pillar splitting does not require notch preparation or crack length measurement, and is less affected by residual stresses [29,44]. Due to its ease of implementation and robustness, pillar splitting has been widely applied, for example, to investigate hard coatings [45], oxide films [1], and battery materials [6,7,14]. Nonetheless, evaluating the fracture toughness requires non-linear finite element analysis for materials with different E/H ratios, and uncertainties arise from the complex triaxial stress field generated beneath the indenter.

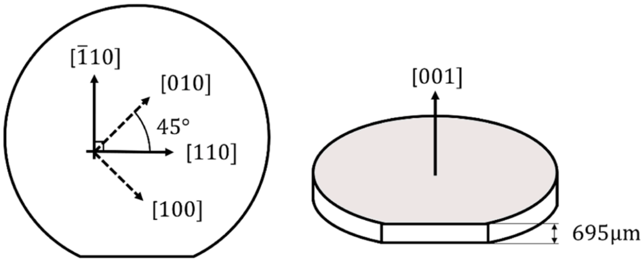

Fig. 2. Schematic of the single-crystal (001) silicon wafer.

These microscale test approaches all have practical and conceptual limitations. They rely on mechanical assumptions that in practice are often only approximately satisfied. Recent work has used machine learning models trained on finite element or combined simulation-experiment data to learn these relations for specific small-scale geometries, including microcantilever bending [46,47] and pillar-splitting [48]. However, the tests themselves still have strict geometric constraints and require precisely controlled loading. These studies improve the numerical evaluation of critical mode I stress intensity factor (i.e. the fracture toughness) for their respective configurations but remain tied to particular specimen designs. FIB-based specimen preparation offers site specificity and precise geometry, but the multi-stage milling and post-processing steps are complex and can be difficult to reproduce.

In this context, the study by Koko et al. [49] introduced a new strategy that goes beyond the limitations of standard specimen geometries. They investigated the cleavage fracture of a brittle material (single crystal silicon) by applying in-situ high (angular) resolution electron backscatter diffraction (HR-EBSD) to observe quasi-static crack propagation, and then directly utilised the full-field strain maps local to the crack tip to evaluate the mixed mode stress intensity factors and fracture toughness.

The present work seeks to develop a simple micromechanical testing approach that leverages full-field elastic strain data to determine the fracture toughness. A novel double-indentation method creates the conditions for controlled initiation, propagation and arrest of a critical crack. In conventional tests, the radial cracks that propagate from a single indentation arrest in the declining stress field that is induced by the elastic and plastic deformation at the indenter contact. The stress field changes when the indenter is removed, and any cracks become sub-critical. However, a suitably positioned subsequent indentation may introduce a radial crack that propagates and arrests in the dominant field of the first indentation. If the effect of the second indent on the stress field is sufficiently small, it is assumed that the arrested crack remains in a near critical state after the removal of the indentation load. HR-EBSD measurement of the full-field elastic strains then allows the crack-tip condition to be accurately quantified at the arrest point, from which the fracture toughness may be obtained. Applied here to cleavage of single-crystal silicon, the method yields crack-tip fields consistent with a near critical arrest state and offers a pathway toward a more universal method to study microstructurally governed fracture at the local scale in polycrystalline materials by in situ observation of the local crack field.

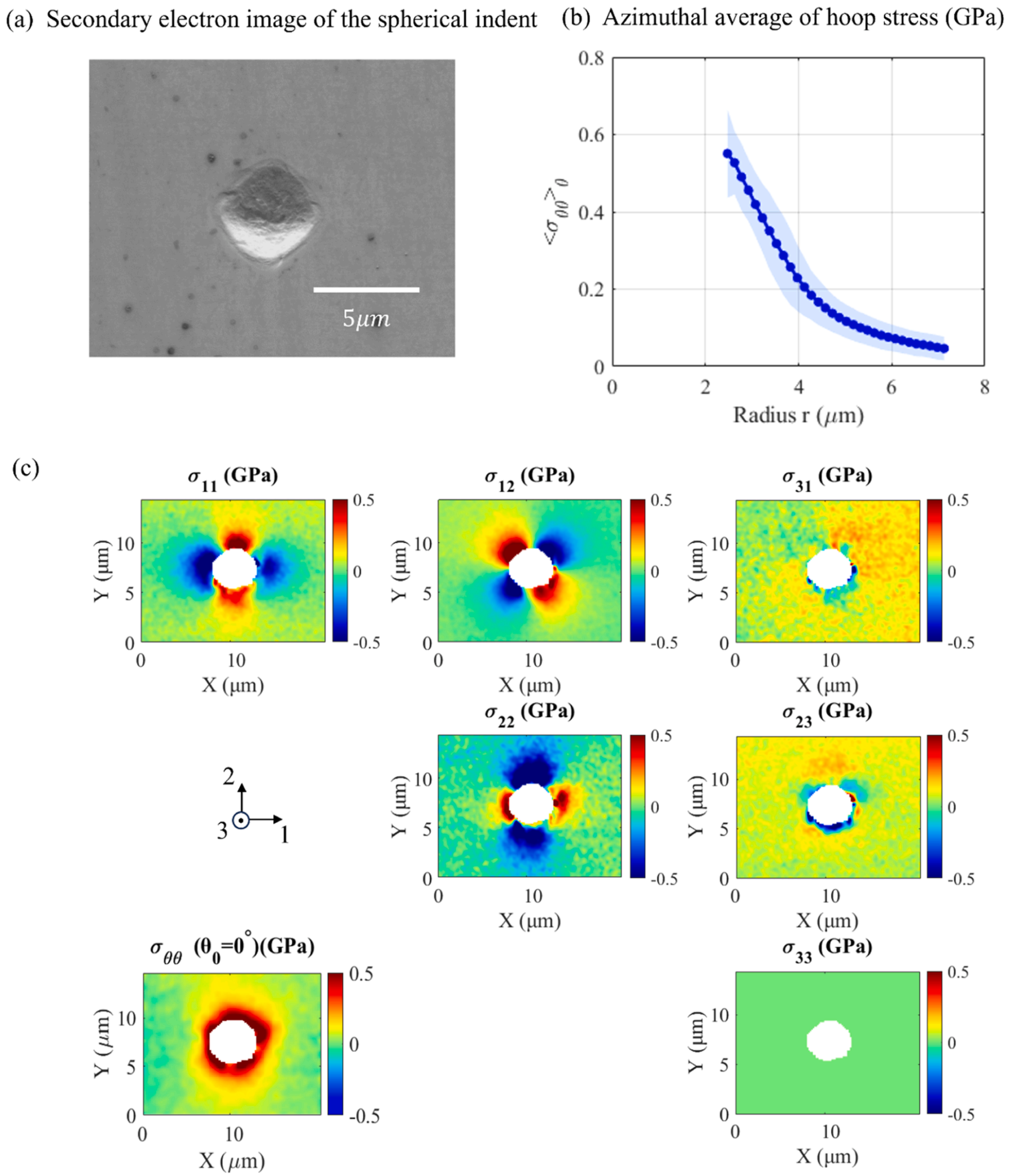

Fig. 3. Residual stress field generated by a 600 nm depth spherical indent on Si(001), measured by HR-EBSD (0.15 μm step size) and calculated with an anisotropic elastic model. (a) Secondary electron (SE) image of the spherical indent, captured at a tilted position. (b) Azimuthally averaged hoop stress as a function of radial distance from the indent. Data start at the average indent edge radius (2.5 μm). The shaded band is one standard deviation in each of the radial bins (annular width = 0.75 μm). (c) Full residual stress tensor field, together with an in-plane hoop stress map (bottom left, plotted in polar coordinates centred at the indent, with θ = 0° along the positive x-axis).

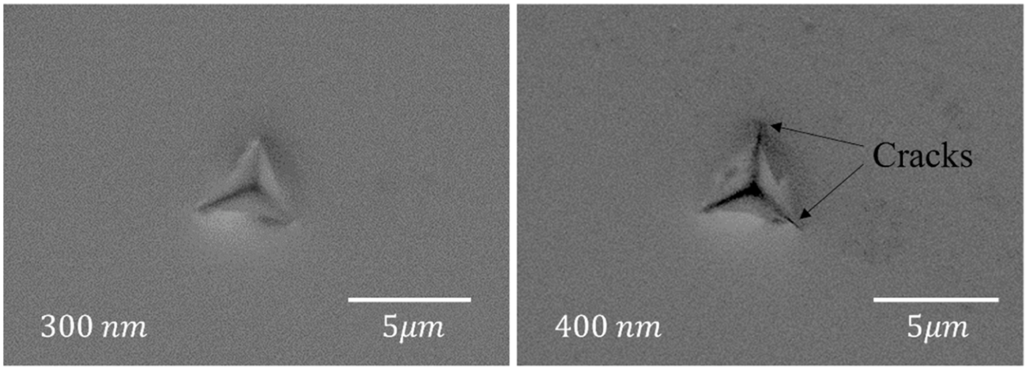

Fig. 4. SE images of Berkovich indentation tests. The applied depth is marked in the lower left corner of each image: (a) 300 nm indent showing no crack initiation at the corners, and (b) 400 nm indent with corner cracks.

2. Experimental method

2.1. Material and nano-indentation

The material was a single-crystal silicon n-type wafer with (001) crystallographic orientation and a thickness of approximately 696 μm (Fig. 2). At room temperature, crack propagation in silicon is governed by brittle cleavage with negligible plasticity. This material (P-doped, nominal resistivity of 90.0 Ω · cm) is widely employed in both electronics and micromechanical testing due to its well-defined structure and consistent mechanical response. It has a cubic structure with preferred cleavage on {111} or {110} [50,51]. Spherical nano-indentation in silicon can generate a residual stress field, without cracking, around the contact zone [52,53], while Berkovich nano-indentation readily initiates radial cracks at its sharply defined corners [50,54]. The single-crystal nature of the wafer enabled alignment of the indenter to facilitate fracture along the intended {111} plane.

The as-received surface was mirror-flat and required no further preparations. Its crystallographic regularity enabled easy alignment using the edges of the fractured samples as a reference. The wafer was sectioned into specimens approximately 6 mm × 6 mm in size and mounted on pin stubs using Agar Scientific's Electrodag 1415 conductive adhesive.

Nanoindentation was conducted using an Agilent G200 Nano Indenter® equipped with diamond Berkovich and spherical tips (Synton-MDP Ltd.). The Berkovich tip had a nominal radius of 20 μm, while the spherical tip had a nominal radius of 10 μm. The instrument was operated in quasi-static mode, following the Oliver and Pharr method [55]. Indentations were performed in displacement-controlled mode with maximum penetration depths set for each test. Typical depths were 600 nm for the spherical tip and 300 or 400 nm for the Berkovich tip. A constant strain rate of 0.05 s^{-1} was applied, with a 5 s dwell at peak for drift correction. Preliminary tests showed that isolated indentations to depths up to 600 nm and 300 nm did not initiate cracks for the spherical and Berkovich tips respectively.

2.2. Full field elastic strain mapping by HR-EBSD

EBSD measurements used a Carl Zeiss® Merlin field emission gun scanning electron microscope (FEG-SEM), equipped with an Oxford Instruments Symmetry® detector featuring a high-resolution CMOS sensor for electron backscatter pattern (EBSP) acquisition. All scans were conducted under an accelerating voltage of 20 kV, a beam current of 10 nA, and a working distance of 18.5 mm. EBSPs were collected in high-resolution mode with an image resolution of 1244 × 1024 pixels.

Two scan configurations were employed depending on the field of view:

- For large-area mapping, the scan field fully captured the dual-indent region. A step size in the range of 0.15 μm − 0.20 μm was used over a grid of approximately 160 × 120 steps, resulting in a mapped area of $\sim 32\ \mu$m × 24 μm. The exposure time was 5 ms − 10 ms per pattern without frame averaging.
- For high-resolution mapping near crack tips, a smaller field of view was adopted. A step size of 60 nm was applied (50 nm in Test A) over a scan grid of approximately 160 × 120 steps, yielding a mapped area of $\sim 9.6\ \mu$m × 7.2 μm. A longer exposure time of 10 ms was used, also without frame averaging, to ensure high-quality pattern acquisition.

The elastic strain field was extracted from the EBSPs using the software CrossCourt® Rapide v4.6, which follows an iterative cross-correlation procedure between EBSPs and a reference pattern (EBSP$_0$), obtained approximately 8 μm remote from the indent edge and assumed to be strain-free. FFT filtering in CrossCourt® Rapide v4.6 suppressed low- and high-frequency noise and improved pattern clarity. The strain tensors were calculated from the deformation gradient field under the assumption of plane-stress boundary conditions and elastic anisotropy of the single crystal (C_{11} = 165.78 GPa, C_{12} = 63.94 GPa, and C_{44} = 79.62 GPa).

2.3. Analysis of crack fields

The elastic strain energy release rate was evaluated as the J-integral, which was calculated from the full field map of the elastic strains obtained by HR-EBSD. Following the method of Koko et al. [49,56], an auxiliary vector field $\boldsymbol{q}_1$ was defined to localise the propagation path, and the Equivalent Domain Integral (EDI) method was applied over the measurement region. The strain energy density was computed from the Green-Lagrangian strain tensor, derived from the deformation gradient.

Specifically, the mode-specific deviatoric-strain tensors ε_{ij}^{M} and the elastic stress tensors σ_{ij}^{M} are related through Hooke's law, which accounts for anisotropic material behaviour using the stiffness matrix. The strain energy density associated with each mode was calculated, and the mode I, II, III stress intensity factors and the effective K can be calculated directly from the decomposed J-integrals.

$$J = J_{\mathrm{I}} + J_{\mathrm{II}} + J_{\mathrm{III}} = \frac{K_{\mathrm{I}}^2}{E} + \frac{K_{\mathrm{II}}^2}{E} + \frac{K_{\mathrm{III}}^2}{2\mu} \quad (1)$$

3. Results

Fig. 3 presents the residual stress field surrounding a typical single spherical nano-indentation, obtained by HR-EBSD strain mapping. The indentation, which did not initiate cracks, is surrounded by a tensile hoop stress field that decays over a distance of several μm from the

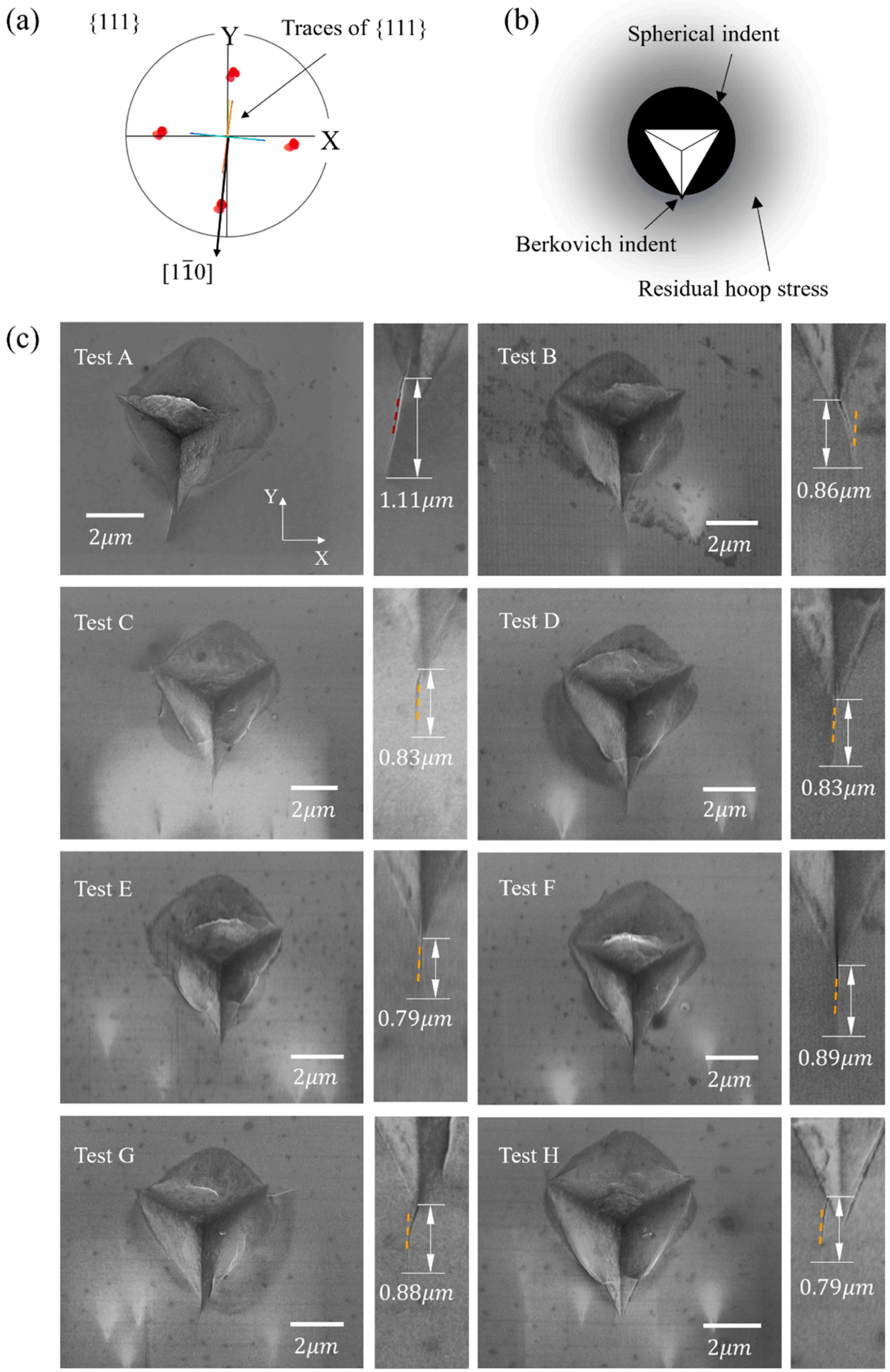

Fig. 5. (a) {111} pole figure showing the crystallographic orientation. (b) Schematic of the experimental design: a second Berkovich nano-indent is positioned inside a spherical nano-indent. (c) SE images of eight dual-indentation tests (A-H). The zoomed images highlight the crack tip and the {111} trace. The measured crack lengths are marked on each image.

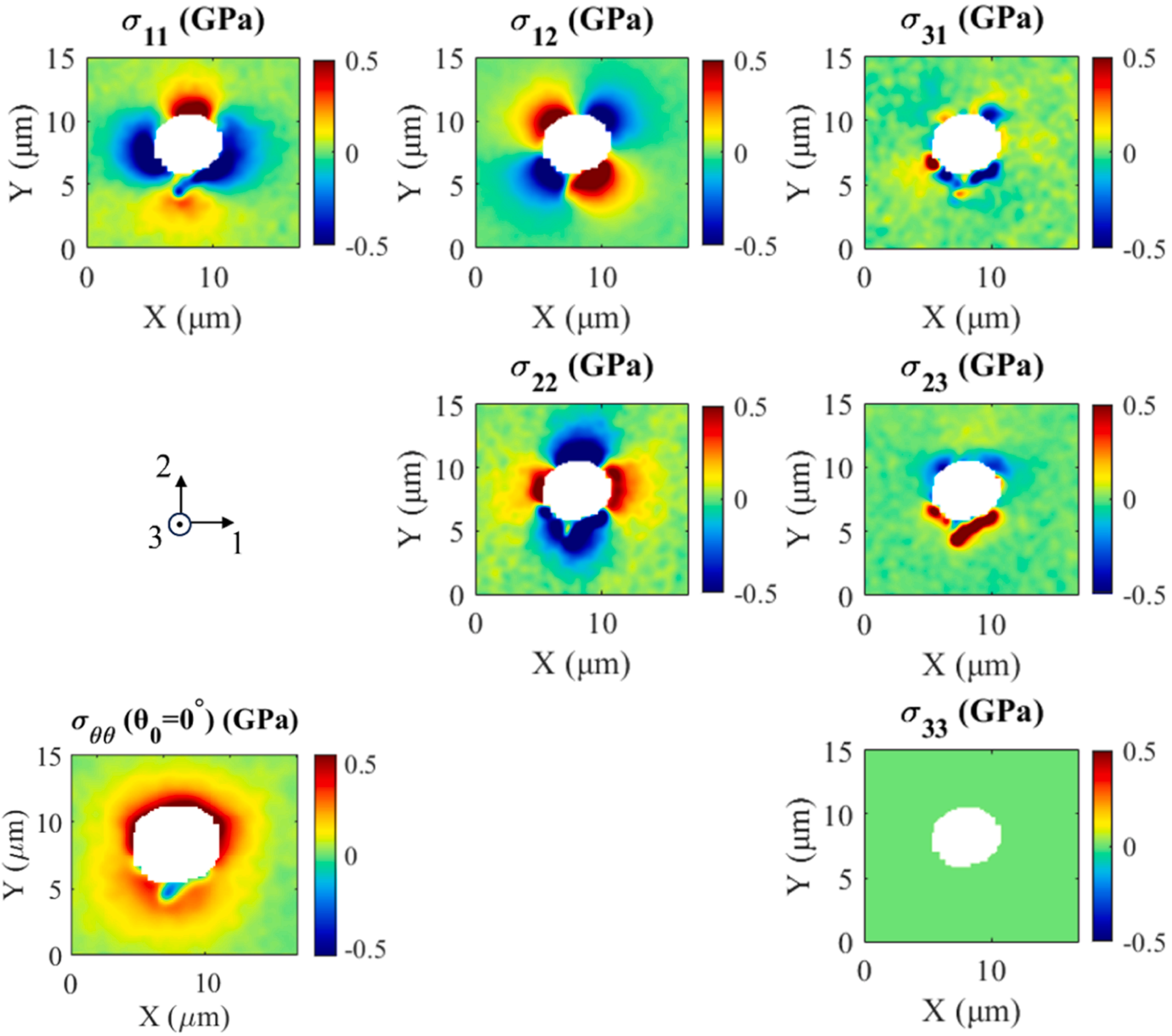

Fig. 6. Full-field stress tensor components around the indent pair in Test A, measured by HR-EBSD with a step size of 0.15 μm, together with an in-plane hoop stress map (bottom left, plotted in polar coordinates centred at the indent, with θ = 0° along the positive x-axis).

indent. Spherical indentations to greater depth generally caused radial cracks. Fig. 4 shows that for single Berkovich indentations, cracks did not initiate if they were sufficiently shallow.

Fig. 5 shows secondary electron (SE) images for double-indentation tests where a Berkovich nano-indent (300 nm depth) was positioned *inside* a previous spherical nano-indent (depth 600 nm or less). One vertex of the Berkovich indenter was aligned parallel to $[1\bar{1}0]$ with its corner at or slightly beyond the edge of the spherical indentation (Fig. 5b). All tests propagated cracks with length of ~1 μm from this corner. These cracks arrested as the residual hoop stress field reduces with increasing distance from the centre of the spherical indent, and it is assumed that, after unloading of the Berkovich indent, the arrested crack remains in a near critical state due to the dominance of the residual stress field of the spherical indentation. The arrested crack tips were aligned with the {111} trace, although in some cases (B and G), the crack initially propagated along a different direction. The arrested crack tips are deduced to be on {111} cleavage planes. The stress fields around the double-indentations were retrieved from HR-EBSD measurements. The example in Fig. 6 shows how the residual field has been partially relaxed by a radial crack from the Berkovich indent (at the 6 o'clock position).

The strain energy release rate and mixed mode stress intensity factors at each arrested crack tip were evaluated via the *J*-integral from the HR-EBSD measurements, following the equivalent domain integral and mode decomposition method of Koko et al. [49]. Fig. 7 illustrates the construction of the contour domain for the integral analysis. High-resolution mapping was used, with a step size of 60 nm in all tests and 50 nm in Test A (shown). This step size defines the spatial resolution of the measured strain field, and a series of closed contours were defined at one-pixel intervals around the crack tip. The representative contour shown (No. 10) lies approximately 0.5 μm from the crack tip. For these contours, Fig. 8 presents the corresponding values obtained for Test A, with data for the other tests provided in the Supplementary Information. Convergence was achieved at approximately 0.5 μm from the crack tip, and the mean and standard error of the *J*-integral and mixed mode stress intensity factors (Table 1) were obtained from contours beyond this. The stress intensity factors of the cracks are predominantly mode I, with contributions from modes II and III. The pixel-level precision of integral analysis was estimated from a crack-free region of each map and used to

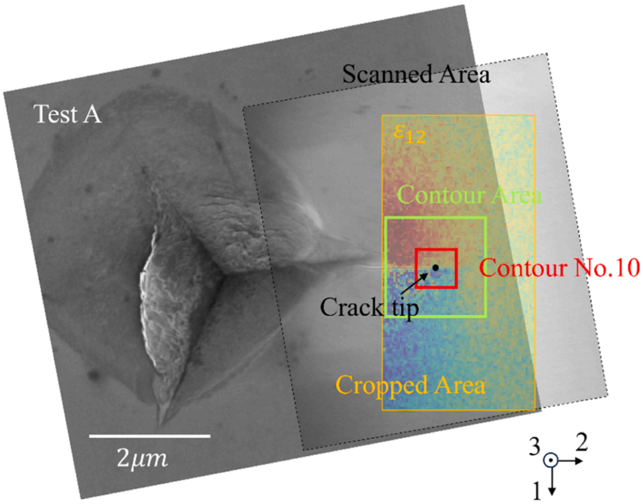

Fig. 7. Montage showing the SE image of the dual indents, the HR-EBSD mapped area around the crack tip and a cropped region of the strain field (in-plane shear $\boldsymbol{\varepsilon}_{12}$), centred at the crack tip. The contour domain is bounded by the indent edge. The crack-tip position and a representative contour (No. 10) are shown. (The data are rotated with the crack aligned horizontally to facilitate the ***J***-integral analysis).

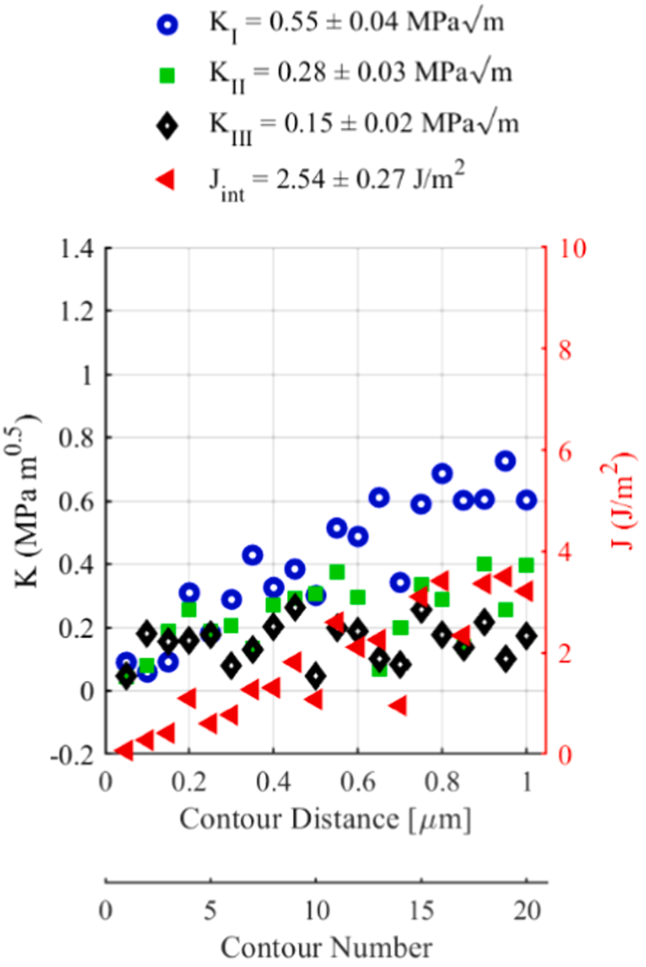

Fig. 8. The ***J***-integral and mode I, II, and III stress-intensity factors with contour size (example data, Test A).

assess the propagated uncertainty in the final results. This estimate (~0.01) is consistent with the contour-to-contour scatter and supports reporting the values in Table 1 to two decimal places.

The effect of the mixed mode loading on fracture propagation was analysed using an energy-based fracture criterion. For two dimensional mode I/II loading, several well established criteria have been proposed, including the Maximum Tangential Stress (MTS) criterion [57], the Minimum Strain Energy Density (MSED) approach [58], and the Maximum Energy Release Rate (MERR) criterion [59–62], all of which have been widely used to describe mixed mode crack paths and initiation conditions. The present indentation cracks, however, experience general mode I/II/III loading. Direct extensions of MTS and MSED to three dimensions show limited sensitivity to mode III and may provide inconsistent predictions when out of plane shear is dominant. Chang et al. [63] therefore built on the MERR concept [59–62] to formulate a unified three dimensional fracture criterion. Their Maximum Potential Energy Release Rate (MPERR) framework recovers the classical mixed mode I/II limits and maps arbitrary I/II/III loading onto a single effective stress intensity factor. In this framework, the mixed mode fracture condition is expressed as

$$\left(\frac{K_{\mathrm{I}}}{K_{\mathrm{Ic}}}\right)^2+\left(\frac{K_{\mathrm{II}}}{K_{\mathrm{IIc}}}\right)^2+\left(\frac{K_{\mathrm{III}}}{K_{\mathrm{IIIc}}}\right)^2=1 \tag{2}$$

Here K_{IC}, K_{IIC}, K_{IIIC} represent the critical stress intensity factors in pure mode I, II, and III, respectively, which can be expressed relative to an effective toughness K_{eff}:

$$K_{\mathrm{Ic}}=K_{\mathrm{eff}},\quad K_{\mathrm{IIc}}=\frac{\sqrt{3}}{2}K_{\mathrm{Ic}},\quad K_{\mathrm{IIIc}}=\frac{\sqrt{k+1}}{2}K_{\mathrm{Ic}} \tag{3}$$

Where k accounts for Poisson's ratio under plane stress conditions:

$$k=\frac{3-\nu}{1+\nu} \tag{4}$$

An optimal critical mode I stress intensity factor $K_{\mathrm{Ic}}^{\mathrm{opt}}$ was determined through a least-squares fit of the experimental data to the three-dimensional MPERR surface (Fig. 9) defined by

$$K_{\mathrm{Ic}}^{\mathrm{opt}}=\underset{K_{\mathrm{Ic}}}{\operatorname{argmin}}\sum_{i=1}^{n}\left[\left(\frac{K_{\mathrm{I}}^{(i)}}{K_{\mathrm{Ic}}}\right)^2+\left(\frac{K_{\mathrm{II}}^{(i)}}{K_{\mathrm{IIc}}}\right)^2+\left(\frac{K_{\mathrm{III}}^{(i)}}{K_{\mathrm{IIIc}}}\right)^2-1\right]^2 \tag{5}$$

This found $K_{\mathrm{Ic}}^{\mathrm{opt}}=0.70\,\mathrm{MPa\cdot m^{1/2}}$, which is comparable to the mean ($\overline{K_{\mathrm{Ic}}}$) and standard deviation (s) of the test population (Table 1) of $\overline{K_{\mathrm{Ic}}}=0.69\,\mathrm{MPa\cdot m^{1/2}}$ and $s=0.04\,\mathrm{MPa\cdot m^{1/2}}$.

4. Discussion

The fracture toughness for {100}, {110}, and {111} cleavage, reported by Masolin et al. [51], are summarised in Table 2. These were obtained using various experimental techniques, including indentation, four-point bending, and double-cantilever beam (DCB) tests. The {111} cleavage fracture toughness obtained here by HR-EBSD of arrested cracks with double-indentation falls within the expected range and is consistent with the assumed near-critical arrest condition.

The analysed cracks were close to {111} at their arrest, but in some cases they initially propagated along less favourable, higher-energy paths before returning to the energetically preferred {111}. The non-negligible shear close to the Berkovich indent corner can induce crack deflections due to the strong influence of the local strain field on the strain energy release rate. The cracks are thus affected by factors that influence the strain fields, including the indenter orientation relative to the crystal, the anisotropy of elastic properties and the preferred cleavage planes and also the anisotropy of plastic deformation. This is a significant cause of variability, which affects the accuracy of toughness measurement by indentation using analytical models such as Lawn-Evans-Marshall.

Table 1
The $\boldsymbol{J}$-integral, mixed mode stress intensity factors and $\boldsymbol{K_{Ic}}$ obtained using MPERR. Data are mean ± standard error. The number of contours used (n) is shown.

Test	K_{I} (MPa·m$^{1/2}$)	K_{II} (MPa·m$^{1/2}$)	K_{III} (MPa·m$^{1/2}$)	J (J/m^2)	K_{Ic} (*MPERR*) (MPa·m$^{1/2}$)
A ($n = 11$)	0.55 ± 0.04	0.28 ± 0.03	0.15 ± 0.02	2.54 ± 0.27	0.66 ± 0.04
B ($n = 13$)	0.65 ± 0.03	0.17 ± 0.01	0.22 ± 0.02	2.99 ± 0.24	0.72 ± 0.03
C ($n = 6$)	0.65 ± 0.02	0.08 ± 0.01	0.08 ± 0.01	2.48 ± 0.14	0.66 ± 0.02
D ($n = 5$)	0.63 ± 0.03	0.23 ± 0.02	0.11 ± 0.03	2.65 ± 0.29	0.69 ± 0.03
E ($n = 6$)	0.57 ± 0.03	0.15 ± 0.01	0.18 ± 0.04	2.79 ± 0.25	0.63 ± 0.03
F ($n = 9$)	0.70 ± 0.02	0.09 ± 0.02	0.17 ± 0.03	4.06 ± 0.26	0.73 ± 0.02
G ($n = 6$)	0.66 ± 0.02	0.11 ± 0.02	0.10 ± 0.03	3.27 ± 0.22	0.68 ± 0.02
H ($n = 5$)	0.70 ± 0.03	0.12 ± 0.02	0.21 ± 0.03	3.30 ± 0.23	0.75 ± 0.03

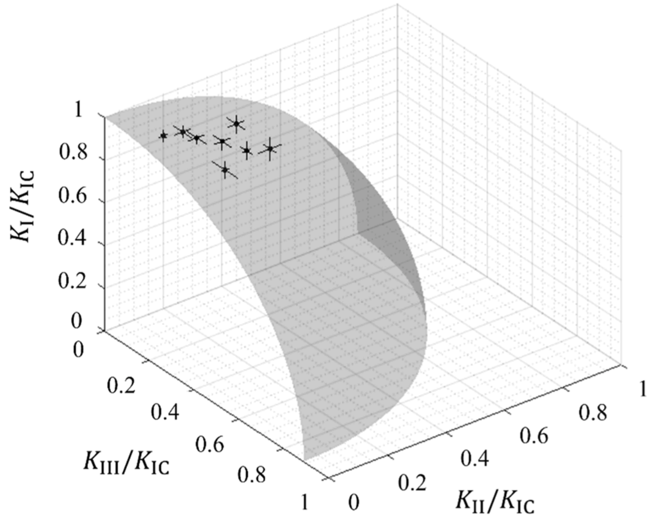

Fig. 9. Three-dimensional fracture surface defined by the MPERR criterion. Experimental data from the double-indentation tests are shown with the optimal surface.

Table 2
Reported mode I fracture toughness values for single crystal silicon cleavage at room temperature (data from [48]).

Fracture Plane	{100}	{110}	{111}
K_{Ic} (MPa·m$^{1/2}$)	0.75–1.29	0.68–1.19	0.62–1.22

The evaluation of the strain fields of arrested cracks by high-resolution HR-EBSD mapping directly addresses this limitation. It enables decomposition of the crack-tip fields into mode I, II, and III stress intensity factors from which the effective mode I stress intensity factor can be determined. The application of double-indentation to propagate and arrest cracks in a stable and dominant residual stress field provided crack tips in the same critical condition, demonstrated by the small coefficient of variation ($\sim 6\%$) across tests that produced cracks of varying length due to inherent variations in the indenter contact and orientation.

The double-indentation approach offers several practical advantages. First, it retains the simplicity of conventional indentation testing, requiring no elaborate specimen preparation while remaining straightforward to implement. Second, it provides a controlled means of driving and arresting cracks in a critical state to enable the direct evaluation of the fracture toughness. This does not rely on the assumption of pure mode I loading, nor on measurement of crack lengths, both of which are limitations of existing toughness measurement methods. This represents a significant advancement in the evaluation of cleavage toughness, enabling a more reliable and broadly applicable assessment.

In the present study, near-surface HR-EBSD measurements of the full elastic strain tensor were obtained, from which the local mixed-mode fracture parameters were determined. The crack develops a three-dimensional geometry that depends on the local sub-surface strain fields, and a full three-dimensional description of the crack-tip field would require volumetric mapping techniques. However, the propagation vector of the studied cracks is in the surface plane, and the path independence of the energy integrals supports interpreting these values as the local fracture driving force at the observed surface.

The present implementation is restricted to cleavage fracture in brittle materials, as demonstrated here for single crystal silicon. In this regime the crack tip fields measured by HR-EBSD can be interpreted within linear elastic fracture mechanics. In theory, if a material exhibits only limited plasticity and the small-scale yielding conditions are satisfied, evaluating the integrals in the K-controlled region would still provide an effective measure of the crack tip fracture driving force. However, in microscale fracture toughness testing the specimen dimensions are typically very small and the small-scale yielding assumption is difficult to satisfy. In such cases an elastic-plastic fracture mechanics treatment is required, with an explicit description of the inelastic process zone, which lies beyond the scope of the present work. In contrast, residual elastic stresses are naturally included in the present framework because the energy integrals are evaluated from the total elastic field. For brittle systems, the critical fracture parameters at crack extension are not affected by whether the crack is driven by externally applied loads or by residual stresses.

In principle, this approach could be applied to intergranular fracture, where indentation-driven cracks propagate along inclined paths between grains and experience mixed-mode loading. There is a critical need for data on the relationships between grain boundary structure (i.e. ‘complexion’ [64]) and fracture toughness to support microstructure design of high performance ceramics by multi-scale models [65]. There are some challenges, but these are not insurmountable. The calculation of the path-independent integral for propagation along interfaces between grains of different elastic moduli could be addressed by approaches such as separated integrals [66]. The selection of an appropriate stress-free reference for HR-EBSD will be difficult in fine grained microstructures, but this could be addressed by absolute lattice-parameter simulation (e.g. [67,68]) or measurement (e.g. [69]). In-situ HR-EBSD to observe stable cracks from single indents whilst under load would be the optimal approach to characterise critical cracks, as this would remove the assumption that the unloading of the second indentation has negligible effect. This would require the design of an in-SEM nanoindenter that was compatible with the constraints of HR-EBSD (i.e. high tilt angle). Double-indentation, used here in the absence of a capability for in-situ observations, could be applied to polycrystalline ceramics, but with reduced confidence that the cracks are quite at the critical state.

5. Conclusion

This study presented a novel methodology to evaluate the cleavage fracture toughness by analysis of critical arrested cracks. The approach overcomes key limitations of conventional indentation methods by enabling cracks to be introduced and arrested under a well-controlled residual stress field, and by directly measuring the crack-tip strain fields through full-field HR-EBSD. Through evaluation of the *J*-integral, the mode-specific stress intensity factors (K_I, K_II, and K_III) can be extracted, and the Maximum Potential Energy Release Rate (MPERR) criterion applied to evaluate the critical mode I fracture toughness. Applied to cleavage in Silicon, the obtained fracture toughness (0.70 MPa·$\mathrm{m}^{1/2}$) was reproducible and consistent with literature data.

Importantly, the methodology requires minimal sample preparation, avoids the need for FIB milling, and retains the simplicity and practicality of indentation-based methods, while achieving a repeatable and high spatial resolution fracture mechanics analysis. As such, this framework lays the foundation for a versatile and reliable tool for micromechanical fracture toughness testing of cleavage planes and grain boundaries in brittle materials.

CRediT authorship contribution statement

Xiao Su: Writing – original draft, Methodology, Investigation, Formal analysis. **Zikang Zhang:** Investigation. **Marcus Williamson:** Investigation. **Marin Vuksic:** Investigation. **Abdalrhaman Koko:** Writing – review & editing, Software. **T. James Marrow:** Writing – review & editing, Supervision, Conceptualization.

Declaration of competing interest

The authors declare that they have no known competing financial interests or personal relationships that could have appeared to influence the work reported in this paper.

Acknowledgements

We are grateful to Professor R S Bonilla (University of Oxford) for supplying the specimen material and Dr G. Meaden (BLG Vantage) for support with the CrossCourt software. The authors acknowledge the use of characterisation facilities within the David Cockayne Centre for Electron Microscopy (DCCEM), Department of Materials, University of Oxford, alongside financial support provided by the Henry Royce Institute (Grant ref EP/R010145/1).

Supplementary materials

Supplementary material associated with this article can be found, in the online version, at doi:10.1016/j.actamat.2025.121797.

References

[1] G. Bolelli, et al., Damage progression in thermal barrier coating systems during thermal cycling: a nano-mechanical assessment, Mater. Des. 166 (2019) 107615, https://doi.org/10.1016/j.matdes.2019.107615, 2019/03/15/.

[2] N.P. Padture, M. Gell, E.H. Jordan, Thermal barrier coatings for gas-turbine engine applications, Science (1979) 296 (5566) (2002) 280–284, https://doi.org/10.1126/science.1068609.

[3] F.P.E. Dunne, D. Rugg, On the mechanisms of fatigue facet nucleation in titanium alloys, Fatigue Fract. Eng. M 31 (11) (2008) 949–958, https://doi.org/10.1111/j.1460-2695.2008.01284.x.

[4] C. Wu, C. Wei, Y. Li, In situ mechanical characterization of the mixed-mode fracture strength of the Cu/Si interface for TSV structures, Micromachines. (Basel) 10 (2) (2019) 86 [Online]. Available: https://www.mdpi.com/2072-666X/10/2/86.

[5] L. Xi, C. Qiao, D. Pradeep, C. Ritwik, R.R. Tummala, S.K. Sitaraman, Failure mechanisms and optimum design for electroplated copper through-Silicon vias (TSV), in: 2009 59th Electronic Components and Technology Conference 2009, 2009, pp. 624–629, https://doi.org/10.1109/ECTC.2009.5074078, 26-29 May.

[6] A.-N. Wang, J.F. Nonemacher, G. Yan, M. Finsterbusch, J. Malzbender, M. Krüger, Mechanical properties of the solid electrolyte Al-substituted Li7La3Zr2O12 (LLZO) by utilizing micro-pillar indentation splitting test, J. Eur. Ceram. Soc. 38 (9) (2018) 3201–3209, https://doi.org/10.1016/j.jeurceramsoc.2018.02.032, 2018/08/01/.

[7] M.Z. Mughal, R. Moscatelli, H.-Y. Amanieu, M. Sebastiani, Effect of lithiation on micro-scale fracture toughness of LixMn2O4 cathode, Scr. Mater. 116 (2016) 62–66, https://doi.org/10.1016/j.scriptamat.2016.01.023, 2016/04/15/.

[8] D. Chen, X.-F. Zhang, R.O. Ritchie, Effects of grain-boundary structure on the strength, toughness, and cyclic-fatigue properties of a monolithic silicon carbide, J. Am. Ceramic Soc. 83 (8) (2000) 2079–2081, https://doi.org/10.1111/j.1151-2916.2000.tb01515.x.

[9] N. Al Nasiri, N. Ni, E. Saiz, J. Chevalier, F. Giuliani, L.J. Vandeperre, Effect of microstructure and grain boundary chemistry on slow crack growth in silicon carbide at ambient conditions, J. Eur. Ceram. Soc. 35 (8) (2015) 2253–2260, https://doi.org/10.1016/j.jeurceramsoc.2015.02.020, 2015/08/01/.

[10] J.P. Parmigiani, M.D. Thouless, The roles of toughness and cohesive strength on crack deflection at interfaces, J. Mech. Phys. Solids. 54 (2) (2006) 266–287, https://doi.org/10.1016/j.jmps.2005.09.002, 2006/02/01/.

[11] A.G. EVANS, K.T. FABER, Toughening of ceramics by circumferential microcracking, J. Am. Ceramic Soc. 64 (7) (1981) 394–398, https://doi.org/10.1111/j.1151-2916.1981.tb09877.x.

[12] J.P. Best, Z. Johannes, W.J. M, S. Rachel, M. Marcus, J. Michler, Small-scale fracture toughness of ceramic thin films: the effects of specimen geometry, ion beam notching and high temperature on chromium nitride toughness evaluation, Philosoph. Magaz. 96 (32–34) (2016) 3552–3569, https://doi.org/10.1080/14786435.2016.1223891, 2016/12/01.

[13] J. Schaufler, C. Schmid, K. Durst, M. Göken, Determination of the interfacial strength and fracture toughness of a-C:h coatings by in-situ microcantilever bending, Thin. Solid. Films. 522 (2012) 480–484, https://doi.org/10.1016/j.tsf.2012.08.031, 2012/11/01/.

[14] M.Z. Mughal, H.-Y. Amanieu, R. Moscatelli, M. Sebastiani, A comparison of microscale techniques for determining fracture toughness of LiMn2O4 particles, Materials. (Basel) 10 (4) (2017) 403 [Online]. Available: https://www.mdpi.com/1996-1944/10/4/403.

[15] V.T. Srikar, S.M. Spearing, A critical review of microscale mechanical testing methods used in the design of microelectromechanical systems, Exp. Mech. 43 (3) (2003) 238–247, https://doi.org/10.1007/BF02410522, 2003/09/01.

[16] B. Lawn, R. Wilshaw, Indentation fracture: principles and applications, J. Mater. Sci. 10 (6) (1975) 1049–1081, https://doi.org/10.1007/BF00823224, 1975/06/01.

[17] A.G. Evans, E.A. Charles, Fracture toughness determinations by indentation, J. Am. Ceram. Soc. 59 (7–8) (1976) 371–372, https://doi.org/10.1111/j.1151-2916.1976.tb10991.x.

[18] D.B. Marshall, B.R. Lawn, Residual stress effects in sharp contact cracking, J. Mater. Sci. 14 (8) (1979) 2001–2012, https://doi.org/10.1007/BF00551043, 1979/08/01.

[19] B.R. Lawn, A.G. Evans, D.B. Marshall, Elastic/plastic indentation damage in ceramics: the median/radial crack system, J. Am. Ceramic Soc. 63 (9–10) (1980) 574–581, https://doi.org/10.1111/j.1151-2916.1980.tb10768.x.

[20] J.H. Lee, Y.F. Gao, K.E. Johanns, G.M. Pharr, Cohesive interface simulations of indentation cracking as a fracture toughness measurement method for brittle materials, Acta Mater. 60 (15) (2012) 5448–5467, https://doi.org/10.1016/j.actamat.2012.07.011, 2012/09/01/.

[21] M.D. Uchic, D.M. Dimiduk, J.N. Florando, and W.D. Nix, "Sample dimensions influence strength and crystal plasticity," *Science (1979),* Article vol. 305, no. 5686, pp. 986–989, 2004, doi: 10.1126/science.1098993.

[22] O. Kraft, P.A. Gruber, R. Mönig, D. Weygand, Plasticity in confined dimensions, Annu Rev. Mater. Res. 40 (Volume 40) (2010) 293–317, https://doi.org/10.1146/annurev-matsci-082908-145409, 2010.

[23] F. Iqbal, J. Ast, M. Göken, K. Durst, In situ micro-cantilever tests to study fracture properties of NiAl single crystals, Acta Mater. 60 (3) (2012) 1193–1200, https://doi.org/10.1016/j.actamat.2011.10.060, 2012/02/01/.

[24] B. Merle, M. Göken, Fracture toughness of silicon nitride thin films of different thicknesses as measured by bulge tests, Acta Mater. 59 (4) (2011) 1772–1779, https://doi.org/10.1016/j.actamat.2010.11.043, 2011/02/01/.

[25] D.E.J. Armstrong, A.J. Wilkinson, S.G. Roberts, Micro-mechanical measurements of fracture toughness of bismuth embrittled copper grain boundaries, Philos. Mag. Lett. 91 (6) (2011) 394–400, https://doi.org/10.1080/09500839.2011.573813, 2011/06/01.

[26] B.N. Jaya, V. Jayaram, S.K. Biswas, A new method for fracture toughness determination of graded (Pt,Ni)Al bond coats by microbeam bend tests, Philosophic. Magaz. 92 (25–27) (2012) 3326–3345, https://doi.org/10.1080/14786435.2012.669068, 2012/09/01.

[27] S. Liu, J.M. Wheeler, P.R. Howie, X.T. Zeng, J. Michler, W.J. Clegg, Measuring the fracture resistance of hard coatings, Appl. Phys. Lett. 102 (17) (2013), https://doi.org/10.1063/1.4803928.

[28] G. Sernicola, et al., In situ stable crack growth at the micron scale, Nat. Commun. 8 (1) (2017) 108, https://doi.org/10.1038/s41467-017-00139-w, 2017/07/24.

[29] M. Sebastiani, K.E. Johanns, E.G. Herbert, F. Carassiti, G.M. Pharr, A novel pillar indentation splitting test for measuring fracture toughness of thin ceramic coatings, Philosoph. Magaz. 95 (16–18) (2015) 1928–1944, https://doi.org/10.1080/14786435.2014.913110, 2015/06/23.

[30] D.E.J. Armstrong, M.E. Rogers, S.G. Roberts, Micromechanical testing of stress corrosion cracking of individual grain boundaries, Scr. Mater. 61 (7) (2009) 741–743, https://doi.org/10.1016/j.scriptamat.2009.06.017, 2009/10/01/.

[31] H. Dugdale, D.E.J. Armstrong, E. Tarleton, S.G. Roberts, S. Lozano-Perez, How oxidized grain boundaries fail, Acta Mater. 61 (13) (2013) 4707–4713, https://doi.org/10.1016/j.actamat.2013.05.012, 2013/08/01/.

[32] K. Matoy, T. Detzel, M. Müller, C. Motz, G. Dehm, Interface fracture properties of thin films studied by using the micro-cantilever deflection technique, Surface Coat. Technol. 204 (6) (2009) 878–881, https://doi.org/10.1016/j.surfcoat.2009.09.013, 2009/12/25/.

[33] H. Hirakata, Y. Takahashi, D. Van Truong, T. Kitamura, Role of plasticity on interface crack initiation from a free edge and propagation in a nano-component, Int. J. Fract. 145 (4) (2007) 261–271, https://doi.org/10.1007/s10704-007-9079-0, 2007/06/01.

[34] Y. Takahashi, et al., Evaluation of interfacial fracture strength in micro-scale components combined with high-voltage environmental electron microscopy, Exp. Mech. 55 (6) (2015) 1047–1056, https://doi.org/10.1007/s11340-015-0008-2, 2015/07/01.

[35] J. Ast, M. Göken, K. Durst, Size-dependent fracture toughness of tungsten, Acta Mater. 138 (2017) 198–211, https://doi.org/10.1016/j.actamat.2017.07.030, 2017/10/01/.

[36] J. Ast, G. Mohanty, Y. Guo, J. Michler, X. Maeder, In situ micromechanical testing of tungsten micro-cantilevers using HR-EBSD for the assessment of deformation evolution, Mater. Des. 117 (2017) 265–266, https://doi.org/10.1016/j.matdes.2016.12.052, 2017/03/05/.

[37] B.N. Jaya, C. Kirchlechner, G. Dehm, Can microscale fracture tests provide reliable fracture toughness values? A case study in silicon, J. Mater. Res. 30 (5) (2015) 686–698, https://doi.org/10.1557/jmr.2015.2, 2015/03/01.

[38] D.E.J. Armstrong, C.D. Hardie, J.S.K.L. Gibson, A.J. Bushby, P.D. Edmondson, S. G. Roberts, Small-scale characterisation of irradiated nuclear materials: part II nanoindentation and micro-cantilever testing of ion irradiated nuclear materials, J. Nucl. Mater. 462 (2015) 374–381, https://doi.org/10.1016/j.jnucmat.2015.01.053, 2015/07/01/.

[39] C. Bohnert, N.J. Schmitt, S.M. Weygand, O. Kraft, R. Schwaiger, Fracture toughness characterization of single-crystalline tungsten using notched micro-cantilever specimens, Int. J. Plastic. 81 (2016) 1–17, https://doi.org/10.1016/j.ijplas.2016.01.014, 2016/06/01/.

[40] K. Matoy, et al., A comparative micro-cantilever study of the mechanical behavior of silicon based passivation films, Thin. Solid. Films. 518 (1) (2009) 247–256, https://doi.org/10.1016/j.tsf.2009.07.143, 2009/11/02/.

[41] S. Brinckmann, K. Matoy, C. Kirchlechner, G. Dehm, On the influence of microcantilever pre-crack geometries on the apparent fracture toughness of brittle materials, Acta Mater. 136 (2017) 281–287, https://doi.org/10.1016/j.actamat.2017.07.014, 2017/09/01/.

[42] B.N. Jaya, V. Jayaram, Crack stability in edge-notched clamped beam specimens: modeling and experiments, Int. J. Fract. 188 (2) (2014) 213–228, https://doi.org/10.1007/s10704-014-9956-2, 2014/08/01.

[43] H.H. Gatzen, M. Beck, Investigations on the friction force anisotropy of the silicon lattice, Wear. 254 (11) (2003) 1122–1126, https://doi.org/10.1016/S0043-1648(03)00323-5, 2003/10/01/.

[44] M. Sebastiani, K.E. Johanns, E.G. Herbert, G.M. Pharr, Measurement of fracture toughness by nanoindentation methods: recent advances and future challenges, Curr. Opin. Solid State Mater. Sci. 19 (6) (2015) 324–333, https://doi.org/10.1016/j.cossms.2015.04.003, 2015/12/01/.

[45] J.P. Best, J. Wehrs, M. Polyakov, M. Morstein, J. Michler, High temperature fracture toughness of ceramic coatings evaluated using micro-pillar splitting, Scr. Mater. 162 (2019) 190–194, https://doi.org/10.1016/j.scriptamat.2018.11.013, 2019/03/15/.

[46] X. Liu, C.E. Athanasiou, N.P. Padture, B.W. Sheldon, H. Gao, A machine learning approach to fracture mechanics problems, Acta Mater. 190 (2020) 105–112, https://doi.org/10.1016/j.actamat.2020.03.016, 2020/05/15/.

[47] X. Liu, C.E. Athanasiou, N.P. Padture, B.W. Sheldon, H. Gao, Knowledge extraction and transfer in data-driven fracture mechanics, in: Proceedings of the National Academy of Sciences 118, 2021 e2104765118, https://doi.org/10.1073/pnas.2104765118.

[48] C.E. Athanasiou, et al., Integrated simulation, machine learning, and experimental approach to characterizing fracture instability in indentation pillar-splitting of materials, J. Mech. Phys. Solids. 170 (2023) 105092, https://doi.org/10.1016/j.jmps.2022.105092, 2023/01/01/.

[49] A. Koko, T.H. Becker, E. Elmukashfi, N.M. Pugno, A.J. Wilkinson, T.J. Marrow, HR-EBSD analysis of in situ stable crack growth at the micron scale, J. Mech. Phys. Solids. 172 (2023) 105173, https://doi.org/10.1016/j.jmps.2022.105173, 2023/03/01/.

[50] R.F. Cook, Strength and sharp contact fracture of silicon, J. Mater. Sci. 41 (3) (2006) 841–872, https://doi.org/10.1007/s10853-006-6567-y, 2006/02/01.

[51] A. Masolin, P.-O. Bouchard, R. Martini, M. Bernacki, Thermo-mechanical and fracture properties in single-crystal silicon, J. Mater. Sci. 48 (3) (2013) 979–988, https://doi.org/10.1007/s10853-012-6713-7, 2013/02/01.

[52] Y.B. Gerbig, S.J. Stranick, R.F. Cook, Measurement of residual stress field anisotropy at indentations in silicon, Scr. Mater. 63 (5) (2010) 512–515, https://doi.org/10.1016/j.scriptamat.2010.05.017, 2010/09/01/.

[53] A.J. Gayle, et al., Two-dimensional strain-mapping by electron backscatter diffraction and confocal Raman spectroscopy, J. Appl. Phys. 122 (20) (2017), https://doi.org/10.1063/1.5001270.

[54] A. Pajares, M. Chumakov, B.R. Lawn, Strength of silicon containing nanoscale flaws, J. Mater. Res. 19 (2) (2004) 657–660, https://doi.org/10.1557/jmr.2004.19.2.657, 2004/02/01.

[55] W.C. Oliver, G.M. Pharr, An improved technique for determining hardness and elastic modulus using load and displacement sensing indentation experiments, J. Mater. Res. 7 (6) (1992) 1564–1583, https://doi.org/10.1557/JMR.1992.1564, 1992/06/01.

[56] A. Koko, J. Marrow, DIC2Abaqus: calculating mixed-mode stress intensity factors from 2D and 3D-stereo displacement fields, SoftwareX. 31 (2025) 102231, https://doi.org/10.1016/j.softx.2025.102231, 2025/09/01/.

[57] F. Erdogan, G.C. Sih, On the crack extension in plates under plane loading and transverse shear, J. Basic Eng. 85 (4) (1963) 519–525, https://doi.org/10.1115/1.3656897.

[58] G.C. Sih, Strain-energy-density factor applied to mixed mode crack problems, Int. J. Fract. 10 (3) (1974) 305–321, https://doi.org/10.1007/BF00035493, 1974/09/01.

[59] M.A. Hussain, S.L. Pu, and J. Underwood, "Strain energy release rate for a crack under combined mode I and mode II," presented at the 1973 National Symposium on Fracture Mechanics, Part II, Washington, United States, 100 Barr Harbor Drive, PO Box C700, West Conshohocken, PA 19428-2959, 1973, 1973. [Online]. Available: https://hal.science/hal-04166069.

[60] K. Palaniswamy and W.G. Knauss, "***II - on the problem of crack extension in brittle solids under general loading***," in *Mechanics Today*, S. Nemat-Nasser Ed.: Pergamon, 1978, pp. 87–148.

[61] R.J. Nuismer, An energy release rate criterion for mixed mode fracture, Int. J. Fract. 11 (2) (1975) 245–250, https://doi.org/10.1007/BF00038891, 1975/04/01.

[62] C.-H. Wu, Fracture under combined loads by maximum-energy-release-rate criterion, J. Appl. Mech. 45 (3) (1978) 553–558, https://doi.org/10.1115/1.3424360.

[63] J. Chang, J.-q. Xu, Y. Mutoh, A general mixed-mode brittle fracture criterion for cracked materials, Eng. Fract. Mech. 73 (9) (2006) 1249–1263, https://doi.org/10.1016/j.engfracmech.2005.12.011, 2006/06/01/.

[64] S.J. Dillon, M. Tang, W.C. Carter, M.P. Harmer, Complexion: a new concept for kinetic engineering in materials science, Acta Mater. 55 (18) (2007) 6208–6218, https://doi.org/10.1016/j.actamat.2007.07.029, 2007/10/01/.

[65] B. Ye, T. Wen, M.C. Nguyen, L. Hao, C.-Z. Wang, Y. Chu, First-principles study, fabrication and characterization of (Zr0.25Nb0.25Ti0.25V0.25)C high-entropy ceramics, Acta Mater. 170 (2019) 15–23, https://doi.org/10.1016/j.actamat.2019.03.021, 2019/05/15/.

[66] T. Nishioka, S. Syano, T. Fujimoto, Concepts of separated J-integrals, separated energy release rates, and the component separation method of the J-Integral for interfacial fracture mechanics, J. Appl. Mech. 70 (4) (2003) 505–516, https://doi.org/10.1115/1.1576803.

[67] Q. Shi, et al., Towards measuring absolute residual stress by HR-EBSD with simulated reference patterns, Mater. Charact. 218 (2024) 114508, https://doi.org/10.1016/j.matchar.2024.114508, 2024/12/01/.

[68] E.L. Pang, P.M. Larsen, C.A. Schuh, Global optimization for accurate determination of EBSD pattern centers, Ultramicroscopy. 209 (2020) 112876, https://doi.org/10.1016/j.ultramic.2019.112876, 2020/02/01/.

[69] K. Mingard, A. Day, C. Maurice, P. Quested, Towards high accuracy calibration of electron backscatter diffraction systems, Ultramicroscopy. 111 (5) (2011) 320–329, https://doi.org/10.1016/j.ultramic.2011.01.012, 2011/04/01/.